RESEARCH ARTICLE

PHYSICS

Observation of quantum oscillations near the Mott-Ioffe-Regel limit in CaAs$_3$

Yuxiang Wang[1,†], Minhao Zhao[2,†], Jinglei Zhang[3,†], Wenbin Wu[4], Shichao Li[5], Yong Zhang[3], Wenxiang Jiang[6], Nesta Benno Joseph[7], Liangcai Xu[8], Yicheng Mou [1], Yunkun Yang[2], Pengliang Leng[2], Yong Zhang[9], Li Pi[3], Alexey Suslov[10], Mykhaylo Ozerov[10], Jan Wyzula[11], Milan Orlita[11], Fengfeng Zhu[6], Yi Zhang[12], Xufeng Kou[9], Zengwei Zhu[8], Awadhesh Narayan [7], Dong Qian[6], Jinsheng Wen[5], Xiang Yuan[4,13,17,*], Faxian Xiu [1,2,14,15,16,*] and Cheng Zhang [1,15,*]

[1]State Key Laboratory of Surface Physics and Institute for Nanoelectronic Devices and Quantum Computing, Fudan University, Shanghai 200433, China; [2]State Key Laboratory of Surface Physics and Department of Physics, Fudan University, Shanghai 200433, China; [3]Anhui Province Key Laboratory of Condensed Matter Physics at Extreme Conditions, High Magnetic Field Laboratory of the Chinese Academy of Sciences, Hefei 230031, China; [4]State Key Laboratory of Precision Spectroscopy, East China Normal University, Shanghai 200241, China; [5]National Laboratory of Solid State Microstructures and Department of Physics, Nanjing University, Nanjing 210093, China; [6]Key Laboratory of Artificial Structures and Quantum Control (Ministry of Education), School of Physics and Astronomy, Shanghai Jiao Tong University, Shanghai 200240, China; [7]Solid State and Structural Chemistry Unit, Indian Institute of Science, Bangalore 560012, India;

(Continued on next page)

*Corresponding authors. E-mails: xyuan@lps.ecnu.edu.cn; faxian@fudan.edu.cn; zhangcheng@fudan.edu.cn

†Equally contributed to this work.

ABSTRACT

The Mott-Ioffe-Regel limit sets the lower bound of the carrier mean free path for coherent quasiparticle transport. Metallicity beyond this limit is of great interest because it is often closely related to quantum criticality and unconventional superconductivity. Progress along this direction mainly focuses on the strange-metal behaviors originating from the evolution of the quasiparticle scattering rate, such as linear-in-temperature resistivity, while the quasiparticle coherence phenomena in this regime are much less explored due to the short mean free path at the diffusive bound. Here we report the observation of quantum oscillations from Landau quantization near the Mott-Ioffe-Regel limit in CaAs$_3$. Despite the insulator-like temperature dependence of resistivity, CaAs$_3$ presents giant magnetoresistance and prominent Shubnikov–de Haas oscillations from Fermi surfaces, indicating highly coherent band transport. In contrast, quantum oscillation is absent in the magnetic torque. The quasiparticle effective mass increases systematically with magnetic fields, manifesting a much larger value than what is expected based on magneto-infrared spectroscopy. This suggests a strong many-body renormalization effect near the Fermi surface. We find that these unconventional behaviors may be explained by the interplay between the mobility edge and the van Hove singularity, which results in the formation of coherent cyclotron orbits emerging at the diffusive bound. Our results call for further study on the electron correlation effect of the van Hove singularity.

Keywords: Mott-Ioffe-Regel limit, quantum oscillations, van Hove singularity, mobility edge

INTRODUCTION

As described by the Boltzmann theory, diffusive electron transport is based on the long-lived quasiparticles, which treat carriers as electron gases moving semiclassically between positively charged ionic cores. The interaction effects with Bloch lattice potential, as well as other quasiparticles, are enclosed in the renormalized effective mass. The long-lived quasiparticle picture is only valid when the mean free path l exceeds the Fermi wavelength [1,2].

It sets the Mott-Ioffe-Regel (MIR) limit ($k_F l > 1$ with k_F the Fermi wave vector) for metals, below which the quasiparticle is no longer well-defined and a metal-to-insulator transition occurs due to electron localization [3,4]. In recent years, observation of metallicity beyond the MIR limit, especially the strange-metal behavior in strongly correlated materials, challenges such a transitional point of view [5–13]. Owing to its intimate connection with quantum criticality and unconventional superconductivity,

metallicity beyond the MIR limit has been intensively investigated but remains mysterious.

Apart from the temperature dependence of resistivity, the presence of a Fermi surface formed by mobile electrons is another important characteristic of metals. When subjected to an external magnetic field, electrons experience Landau quantization and form cyclotron orbits along the contour of a closed Fermi surface. This leads to a series of magnetic quantum oscillations in conductivity, magnetization and thermoelectricity, which have been established as powerful tools for characterizing Fermi surface properties [14]. In order to generate Landau quantization, electrons should remain phase coherent during the cyclotron period. Consequently, quantum oscillations are typically observed in clean metallic systems with high carrier mobility and long mean free path, including, but not limited to, 2D electron gases [15] and topological materials [16,17]. With the reduction of the mean free path, electrons gradually lose coherence upon scattering within the cycle of an orbit, which eventually eliminates the quantum oscillations at finite temperatures. Beyond the MIR limit, electrons generally become incoherent and are not expected to present quantum oscillations [1,2,18].

Here we report the observation of quantum oscillations and quasiparticle mass enhancement in the vicinity of the MIR limit in $CaAs_3$. $CaAs_3$ belongs to the CaP_3 family of materials, which were predicted to be topological nodal-line semimetals in theory without involving spin-orbit coupling [19,20]. The inclusion of spin-orbit coupling opens a small gap in the nodal-loop. No sign of topological surface states was found in previous photoemission experiments [21]. We performed magneto-transport experiments on $CaAs_3$ bulk crystals in variable temperature inserts with a superconducting magnet (9 T), a water-cooled resistive magnet (38 T) and a hybrid magnet (45.22 T). The crystal surface of the as-grown $CaAs_3$ samples is determined to be the (010) plane using X-ray diffraction, as shown in Fig. S1a. The current was applied in the (010) plane with the magnetic field B perpendicular to the plane.

RESULTS

Figure 1a shows the temperature T dependence of the longitudinal resistivity ρ_{xx} in Sample C1 at zero magnetic field. As T changes from 360 K to 2 K, ρ_{xx} increases exponentially by about three orders of magnitude, showing an insulator-like T dependence similar to previous reports [21]. We employ the Arrhenius equation $\rho = \rho_0 e^{-\Delta/k_B T}$ to quantify the thermal activation behavior of ρ_{xx}. Here, Δ and

k_B are activation energy and the Boltzmann constant, respectively. As illustrated in Fig. 1b, two regimes with distinct activation energies ($\Delta_1 = 147$ meV for 220–360 K, $\Delta_2 = 5.89$ meV for 20–60 K) can be observed in the Arrhenius plot (ln ρ_{xx} vs. $1/T$). Below 20 K, ρ_{xx} gradually deviates from the activation behavior and becomes saturated towards the low-temperature limit (refer to Fig. S1b for the ρ_{xx}-T curve of Sample C2 down to 50 mK). According to the heat capacity data shown in Fig. S1c, no sign of any phase transition is detected in the range of 10–150 K. To help us understand the thermal activation of ρ_{xx}, we measured the bulk electronic structure and band filling of $CaAs_3$ crystals by angle-resolved photoemission spectroscopy (ARPES). The dispersion along the $\Gamma - X$ direction at 10 K is shown in Fig. 1c. No significant variation in the band dispersion is found as the temperature increases to 45 K and 70 K (Fig. S2). The Fermi level is located at roughly 42 meV above the conduction band edge along with a gap of 158 meV, which is also consistent with previous ARPES results obtained in $CaAs_3$ [21]. It suggests that the thermal activation from the valence band to the conduction band accounts for Δ_1 in the range of 220–360 K.

We then present Hall resistivity ρ_{yx} as a function of B in Fig. 1d. ρ_{yx} is linear in B at all temperatures, suggesting that one kind of carrier dominates the transport. Surprisingly, a sign reversal of the Hall slope is observed at around 210 K. By performing linear fitting to the ρ_{yx}-B curves, we extract the Hall coefficient R_H as shown in Fig. 1e, indicating the carrier changing from n- to p-type as T decreases. As shown in Fig. S3, R_H also shows similar activation behavior with ρ_{xx}, which indicates that the activation of resistivity comes from thermally activated carriers. We further measured the Seebeck coefficient (the inset of Fig. 1e), which is consistent with the Hall effect and shows similar sign reversal at around 220 K. Note that the p-type carriers given by the Hall and Seebeck effects at low temperatures contradict the position of Fermi level that intersects the conduction band as observed in ARPES, which will be discussed later. Figure 1f shows the carrier density n_H and mobility μ calculated from the Hall effect from 2.5 K to 180 K. In this p-type regime, n_H decreases monotonously from 3.3×10^{17} cm^{-3} at 180 K down to 4.8×10^{15} cm^{-3} at 2.5 K, while μ shows a dip at 20 K and then increases to 263 cm^2/Vs at 2.5 K. The carrier density of $CaAs_3$ is comparable to intrinsic narrow-gap semiconductors such as InSb [22] and $Hg_{1-x}Cd_xTe$ [23] but its mobility value is much lower. The increase of mobility at low temperatures in Fig. 1f may result from the suppression of phonon scattering as well as electron-electron scattering due to the reduced carrier density.

(Continued from previous page)

[8]Wuhan National High Magnetic Field Center and School of Physics, Huazhong University of Science and Technology, Wuhan 430074, China; [9]School of Information Science and Technology, ShanghaiTech University, Shanghai 201210, China; [10]National High Magnetic Field Laboratory, Tallahassee, FL 32310, USA; [11]LNCMI-CNRS UPR3228, Université Grenoble Alpes, Grenoble Cedex 9 38042, France; [12]International Center for Quantum Materials, School of Physics, Peking University, Beijing 100871, China; [13]School of Physics and Electronic Science, East China Normal University, Shanghai 200241, China; [14]Shanghai Qi Zhi Institute, Shanghai 200232, China; [15]Zhangjiang Fudan International Innovation Center, Fudan University, Shanghai 201210, China; [16]Shanghai Research Center for Quantum Sciences, Shanghai 201315, China and [17]Shanghai Center of Brain-Inspired Intelligent Materials and Devices, East China Normal University, Shanghai 200241, China
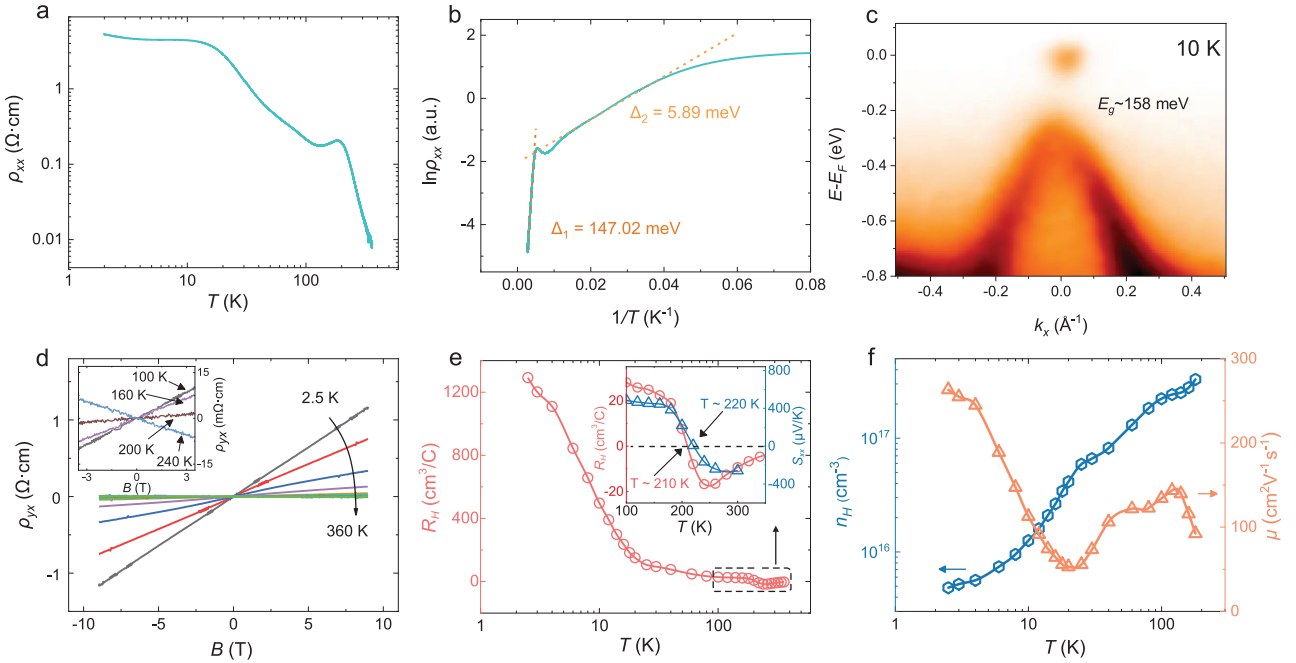
Figure 1. Transport results and ARPES data of CaAs$_3$ crystals. (a) Longitudinal resistivity ρ_{xx} of CaAs$_3$ plotted as a function of temperature (measured in the *a-c* plane). (b) Arrhenius plot of ρ_{xx} with two activation regimes (dashed lines) and the corresponding activation energies. (c) Band dispersion at 10 K measured by ARPES with a photon energy of 98 eV. (d) Hall resistivity curves from 360 K to 2.5 K with the magnetic field perpendicular to the *a-c* plane. The inset is an enlarged view of Hall resistivity curves in the vicinity of the sign reversal. (e) Hall coefficient R_H (derived from the linear fitting of Hall resistivity from −9 T to 9 T) plotted as a function of temperature. The inset is the comparison of the Hall coefficient R_H (circle) and the Seebeck coefficient S_{xx} (triangle), showing similar sign-reversal temperature. (f) The temperature dependence of carrier density (hexagon) and mobility (triangle) below the sign reversal temperature of R_H.

Despite the relatively low mobility, prominent Shubnikov–de Haas (SdH) oscillations and a giant magnetoresistivity (MR) are observed at high magnetic fields up to 38 T. As shown in Fig. 2a, ρ_{xx} starts to oscillate around 7 T and increases by over two orders of magnitude in the range of 20–33 T at 0.3 K. Figure 2b and c display the temperature dependence of the ρ_{xx}-B curves in Samples C1 and C3. The insets of Fig. 2b and c are the extracted SdH oscillations at different temperatures. SdH oscillations decay as temperature rises and gradually smear out above 4 K. We determine the oscillation frequency $F = 23.4$ T and Landau level index n using the Landau fan diagram in Fig. S4b. According to the Onsager relation $F = \frac{\hbar}{2\pi e}A$, the oscillation frequency F is proportional to the cross-sectional area A of the Fermi surface along the direction of B. Here $\hbar$ is the reduced Planck constant and e is the elementary charge. When rotating the magnetic field away from the z direction, SdH oscillations persist as shown in Fig. S6, with characteristics of a 3D Fermi surface. We resolve the Fermi surface anisotropy as a function of θ and φ in Fig. 2d by tracking the oscillation frequency in both the z–y and z–x planes. It corresponds to an ellipsoid-like shape with large out-of-plane anisotropy ($k_z \sim 5k_x$) and weak in-plane

anisotropy ($k_x \sim k_y$), as a result of two Fermi spheres merging together (Fig. S15). It generally agrees with the theoretical curve (the yellow dashed line in Fig. 2d) obtained from the Fermi surface anisotropy given by density functional theory (DFT) calculations. We calculate the in-plane Fermi wave vector as $k_F = 0.0267$ Å^{-1}. Importantly, in stark contrast to the large quantum oscillations and giant MR ratio observed in resistivity, the field dependence of the magnetic torque τ shows neither of these features. In Fig. 2e, we show that de Haas–van Alphen (dHvA) oscillation is also absent as the field rotates. This is contradictory to the general belief that dHvA oscillations are more sensitive to Landau levels than SdH oscillations. In Supplementary Note S3, we exclude the crystal inhomogeneity as the possible origin of the absence of dHvA oscillations. These unusual Landau quantization behaviors in CaAs$_3$ will be discussed in detail later.

SdH oscillations can be quantitatively analyzed using the Lifshitz-Kosevich (LK) formula [14], $\frac{\Delta\rho_{xx}}{\rho_{xx}(B=0)} \propto R_T R_D \cos[2\pi(\frac{F}{B} + \varphi)]$. Note that $R_T = \frac{2\pi^2(k_B T/\hbar\omega)}{\sinh(2\pi^2 k_B T/\hbar\omega)}$ and $R_D = e^{-2\pi^2(k_B T_D/\hbar\omega)}$ are thermal and Dingle damping factors with the cyclotron frequency $\omega = eB/m^*$ and Dingle temperature $T_D = \hbar/2\pi k_B \tau_q$. Here m^*, τ_q and φ are the effective
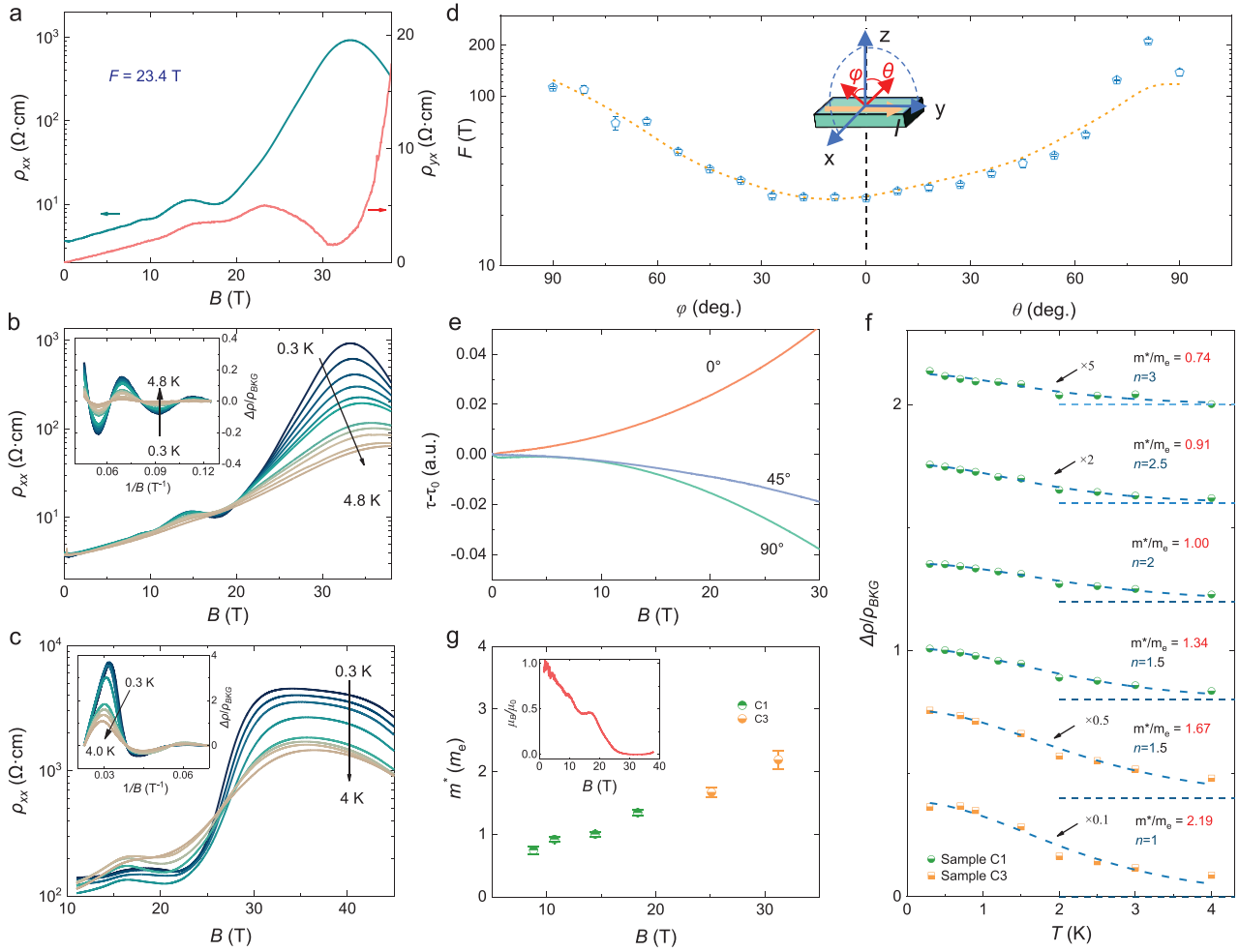
Figure 2. Quantum oscillations observed in high magnetic fields. (a) The magnetic field dependence of ρ_{xx} and ρ_{yx} at 0.3 K with prominent SdH oscillations (Sample C1). The magnetic field is applied perpendicular to the *a-c* plane. (b and c) MR curves of Samples C1 and C3 at different temperatures from 0.3 K to 4.8 K. The inset is the extracted oscillatory component normalized by ρ_{BKG} at different temperatures. (d) The angle dependence of SdH oscillation frequencies of Sample C3. Pentagon dots and the dashed line represent measured data and fitting curve based on the Fermi surface anisotropy given by DFT calculations, respectively. (e) Torque measurement of Sample C3 at different angles at 1.4 K. 0° (90°) represents the magnetic field perpendicular (parallel) to the *a-c* plane. (f) The fitting of the relative resistance change by the temperature factor R_T of the LK formula of Samples C1 and C3 at different fields. Note that it is a stacked view with dashed lines representing the offset values. The effective mass fitting parameter is shown near each curve. (g) The extracted effective mass values of Samples C1 and C3 at different magnetic fields. The inset is the ratio of the mobility values (μ_B/μ_0) in magnetic fields calculated from the Hall angle, where μ_B and μ_0 are the mobility values at a magnetic field of B and zero field, respectively.

mass, quantum lifetime and the phase offset, respectively. In Fig. 2f and Fig. S4d, we employ the LK formula to fit the temperature and magnetic field dependence of SdH oscillations. The oscillation amplitude is obtained by subtracting the MR background, and normalized by ρ_{BKG}. The normalization process is to exclude the influence of large MR background following a recent work [24]. The comparison of different normalization methods is shown in Fig. S5, which only weakly impacts the m^* value. After that, the effective mass m^* at different magnetic fields and Dingle temperature T_D are calculated. Interestingly, m^* systematically increases from $0.74m_e$ at 8.73 T to $2.19m_e$ at 31.25

T (Fig. 2g). To exclude possible influence from MR background subtraction, the increase of m^* with magnetic fields is further verified by the second derivative method and the integral method (refer to Supplementary Note S5). Quasiparticle effective mass is generally determined by the band dispersion as well as interactions with other quasiparticles, which cannot be modulated easily by external magnetic fields. Therefore, the enhancement of quasiparticle effective mass is highly non-trivial and has only been observed in a handful of limited cases such as high-T_c superconductors near the quantum critical point and nodal-loop semimetals upon magnetic breakdown [25–27].
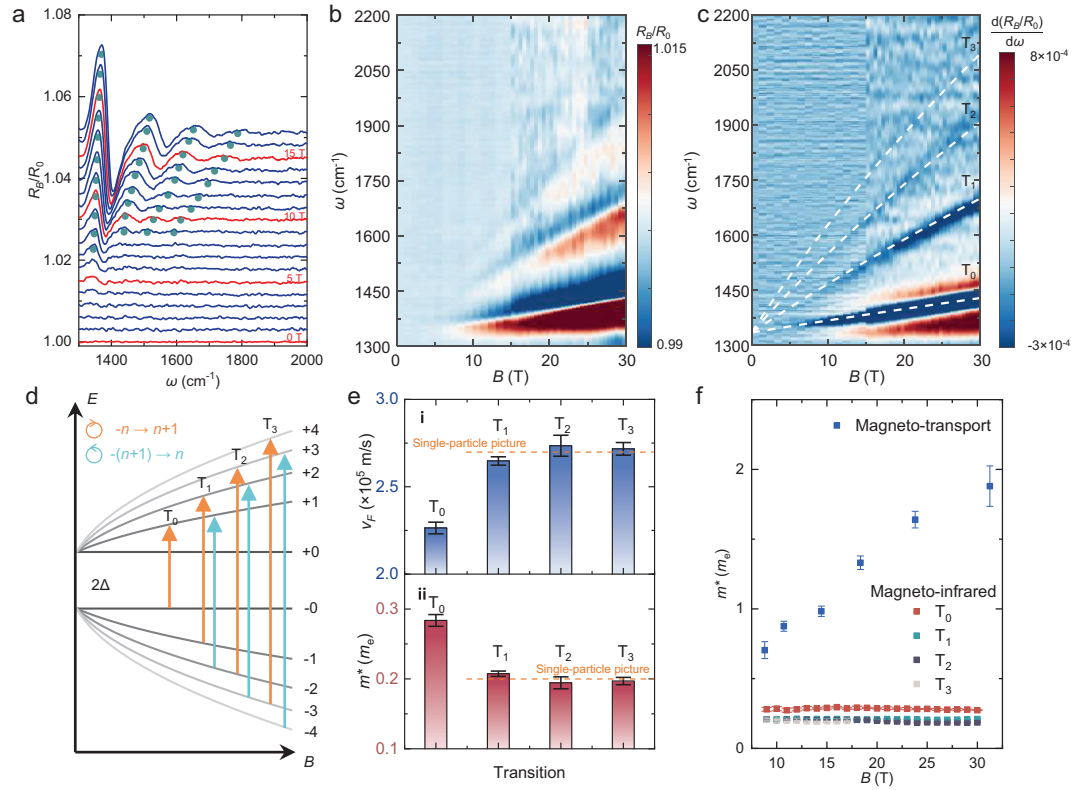
Figure 3. Magneto-infrared spectroscopy of $CaAs_3$. (a) Relative magneto-reflectivity spectra R_B/R_0 measured in a superconducting magnet up to 17 T. All curves are vertically stacked for clarification with a series of interband-Landau-level transitions. The apparent peak features are denoted by green dots. (b) False-color plot of relative magneto-reflectivity spectra in the whole field regime. The spectra for the higher magnetic field are measured in a resistivity magnet. (c) False-color plot of the first-order derivative of relative magneto-reflectivity spectra $d(R_B/R_0)/d\omega$, where the minima are associated with the optical excitation energy. The white dashed curves are the fitting results based on the massive Dirac model. (d) The schematic Landau-level spectrum of $CaAs_3$. The arrows denote the interband-Landau-level transitions with opposite circular polarization. (e) Fermi velocity (panel i) and effective mass (panel ii) fitted from the separate interband-Landau-level transitions. Dashed lines show the Fermi velocity and effective mass obtained from the fitting to a single-particle model. (f) A comparison between effective mass extracted from the quantum oscillations (blue square) and interband-Landau-level transition T_0 (red square). The values of effective mass obtained from the optical transitions T_1 (dark green square), T_2 (dark gray square) and T_3 (light gray square) are less than those from T_0.

By taking the field-dependent value of m^*, the fitting to Dingle damping yields a Dingle temperature of $T_D = 3.9$ K, corresponding to a quantum lifetime of $\tau_q = 3.1 \times 10^{-13}$ s. Then the quantum mean free path is expressed as $l_q = v_F \tau_q = \frac{\hbar k_F \tau_q}{m^*}$, which evolves from 12.9 nm at 8.73 T to 7.1 nm at 18.35 T (Fig. S4). The inset of Fig. 2g shows the ratio of the in-field mobility to its zero-field value, where the in-field value is extracted from the Hall angle $\tan\theta = \mu B$. The ratio dramatically decreases with the increase in B, being consistent with the evolution of l_q. For comparison, we also extract the mean free path from Hall mobility as $l_t = \hbar k_F \mu / e = 4.6$ nm, which is roughly of the same order as l_q, respectively. In Fig. S9, we present the transport results of other $CaAs_3$ samples (C4, C5 and C6), which show consistent transport behaviors of Hall coefficient anomaly and quantum oscillations.

To compare the Landau quantization of $CaAs_3$ in a larger energy range that is less influenced by the many-body interaction, we carried out a magneto-infrared spectroscopy study [28,29]. The relative reflectivity R_B/R_0 is measured on the (010) plane in the Faraday geometry (with B perpendicular to the plane), where R_B and R_0 denote the reflectivity with and without the applied magnetic field, respectively. The spectra measured in a 17.5 T superconducting magnet are presented in Fig. 3a. A larger field range, up to ~30T, is achieved in a resistive coil, and the collected data are shown in a false-color plot (Fig. 3b). A series of prominent peak-to-dip features (peaks are denoted by dark green dots in Fig. 3a) from interband-Landau-level excitations emerge and evolve with B. The observed optical transitions agree with the presence of SdH oscillations in transport and contrast with the unusual absence of quantum

oscillation in magnetic torque. In our data analysis, we associated the minima of $\frac{d(R_B/R_0)}{d\omega}$ [30] with the energies of excitations, as shown in Fig. 3c. All observed interband-Landau-level transitions extrapolate to the same energy in the limit of a vanishing magnetic field. The energy difference between adjacent transitions decreases as a function of the photon energy, thus indicating an unequally spaced Landau levels spectrum. These are typical features of massive Dirac fermions. The corresponding Landau level reads:

$$E_{\pm n} = \pm\sqrt{2e\hbar\,|n|\,Bv_F^2 + \left(\frac{E_g}{2}\right)^2}, \qquad (1)$$

where n is the integer Landau index. The band structure is characterized by the velocity parameter v_F and energy gap E_g. The plus and minus signs denote the Landau levels in the conduction and valence bands, respectively. The selection rule follows $\Delta|n| = \pm 1$ as shown in Fig. 3d, where T_n denotes the $-n \to n+1$ and $-(n+1) \to n$ transitions with the corresponding excitation energy given by:

$$\omega_n(B) = \sqrt{2e\hbar\,(|n|+1)\,Bv_F^2 + \left(\frac{E_g}{2}\right)^2}$$
$$+ \sqrt{2e\hbar\,|n|\,Bv_F^2 + \left(\frac{E_g}{2}\right)^2}. \qquad (2)$$

The white dashed curves shown in Fig. 3c are the best fitting results according to Equation (2) with all transition indices assigned. Due to the absence of splitting for each interband-Landau-level transition, the band structure is expected to be particle-hole symmetric. The overall Fermi velocity is extracted as $v_F = 2.69 \times 10^5$ m/s. The fitted band gap reaches $E_g \sim 165.5$ meV, which is consistent with the gap value extracted from the ARPES as well as the activation energy Δ_1 from the temperature-dependent resistivity. The energy dispersion can be estimated by $E_\pm(k) = E_0 \pm \sqrt{\left(\frac{E_g}{2}\right)^2 + (\hbar v_F k)^2}$, where E_0 defines the zero energy of the low-energy model. The reproduced band dispersion given by magneto-infrared spectroscopy agrees well with the ARPES result (comparison shown in Fig. S7). It further proves that the Landau quantization comes from the gapped bulk band. As shown in Fig. 3e, the Fermi velocity for each set of optical transitions can be separately fitted. The high-index transitions, e.g. $v_F^{T_2}$, $v_F^{T_3}$, are close to the single-particle picture (orange lines in Fig. 3e). In contrast, for the low-index transitions, the extracted $v_F^{T_0}$, $v_F^{T_1}$ as well as m^* deviate away from orange lines. This corresponds to

a Fermi velocity renormalization from a many-body interaction [31–33] for low-energy excitations. Different from the transport measurement where the many-body effect profoundly renormalizes the effective mass near the Fermi energy, the extracted m^* from magneto-infrared spectroscopy by $m^* = \frac{E_g}{2v_F^2}$ (especially for the high-index transition) is less influenced and presents a much smaller value, which is nearly independent of B (Fig. 3f). This is because m^* from magneto-infrared spectroscopy is mainly determined by the Fermi velocity and energy gap of the band. It corresponds to the electronic state property of the entire band due to the much larger detecting energy range compared to transport. Thus, the extracted mass in the infrared spectrum (also known as Dirac mass in the model) corresponds to the single particle mass of the system (refer to Supplementary Note S1 iii). In contrast, the quasiparticle mass from quantum oscillations is sensitive to band structure and interaction effect near Fermi energy. Therefore, the discrepancy between m^* values from magneto-infrared and magneto-transport experiments suggests that the Fermi surface electrons are influenced by a strong renormalization effect, which is also likely to be responsible for the observed mass enhancement in magnetic fields (refer to Supplementary Note S1 for more discussion).

Having obtained the quasiparticle properties of CaAs$_3$, we in turn compare it, in the scaling plot of Fig. 4, with other bulk systems with quantum oscillations from electronic Fermi surfaces. The product of the Fermi wave vector and mean free path, $k_F l$, has been widely used to determine the metallicity of a material. The MIR limit of $k_F l = 1$ defines the mobility edge, below which the electrons become localized [1]. According to the Drude model, the conductivity is expressed as $\sigma = n\mu e = \frac{e^2}{3\pi^2\hbar}k_F^2 l$, which results in the ratio of σ/k_F scaling linearly with the metallicity parameter $k_F l$. Here the ratio of σ/k_F is plotted logarithmically against $k_F l$ over a wide range of 3D bulk materials from high-mobility topological semimetals such as Cd$_3$As$_2$ to narrow-gap semiconductors such as InSb [34–55]. Here the mean free path l is extracted from the Hall mobility. The red dashed line is the theoretical curve given by the Drude model. Note that we mainly focus on materials with simple Fermi surface geometries to avoid complications in $k_F l$ calculation, and materials showing quantum oscillations without bulk electronic Fermi surfaces such as SmB$_6$ and YbB$_{12}$ are also not included [56,57]. Despite the large variation in the carrier density and mobility, the values of σ/k_F and $k_F l$ in these materials converge closely around the red dashed line in Fig. 4, and most materials are located in the deep metallic side with $k_F l \gg 1$.
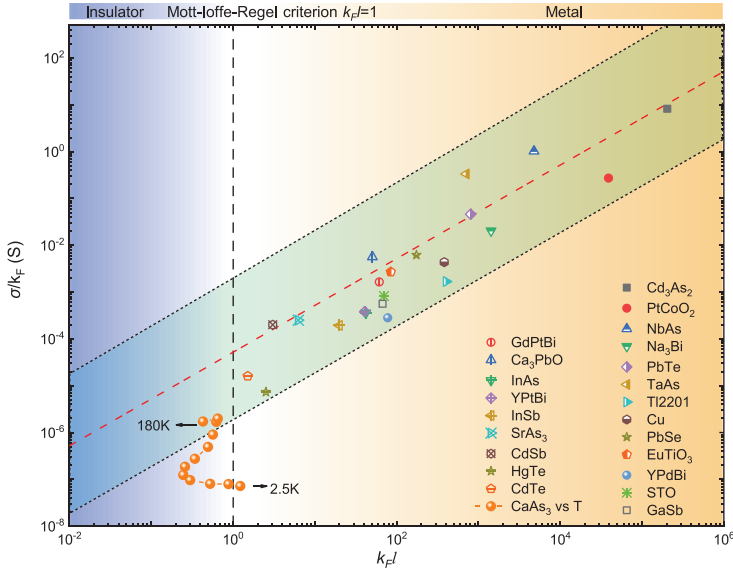
Figure 4. The scaling plot of σ / k_F against the metallicity parameter $k_F l$. The red dashed line is the theoretical curve given by the Drude model. The yellow-white-blue gradient background corresponds to the region with $k_F l \gg 1$, $k_F l \sim 1$ and $k_F l \ll 1$. The black dashed line marks the Mott-Ioffe-Regel limit $k_F l = 1$. The Fermi wave vector k_F was derived from quantum oscillation by the Onsager relation, and the mean free path l was derived from the Fermi wave vector k_F and the Hall mobility μ through $l = \hbar k_F \mu / e$.

In contrast, the transport behavior of CaAs$_3$ significantly deviates from the Drude model as temperature decreases and shows a crossover of the MIR limit. At low temperatures where quantum oscillations emerge, the conductivity of CaAs$_3$ is over two orders of magnitude smaller than the value given by the Drude model. It is also worth mentioning that CaAs$_3$ has the smallest $k_F l$ value ($\sim$1.2 at 2.5 K) among these materials at temperatures where quantum oscillations persist.

Now we summarize the major observations in the transport results of CaAs$_3$: (i) the Hall and Seebeck effects indicate p-type carriers, while the Fermi level crosses the conduction band edge; (ii) strong 3D SdH oscillations with large resistivity appear near the MIR limit, while no dHvA oscillations are observed; (iii) the quasiparticle effective mass given by quantum oscillations increases systematically with magnetic fields and is much larger than that extracted from magneto-infrared spectroscopy. These experimental behaviors violate the standard Fermi liquid picture in the Boltzmann theory and are distinct from conventional narrow-gap semiconductors or band insulators. On the other hand, the coherent transport with Landau quantization and SdH oscillations also differs from typical non-Fermi-liquid systems, in which electrons often become incoherent. The metallicity parameter $k_F l$ close to the MIR limit

suggests that transport in CaAs$_3$ is near the diffusive bound.

DISCUSSION

To explain the aforementioned behaviors, we propose a phenomenological model, as shown in Fig. 5. Figure 5a is a sketch of the bands and density of states (DOS) in CaAs$_3$. The yellow and light-blue regions separated by the mobility edge represent the extended and localized states, respectively, and the orange region corresponds to conducting carriers of the extended states near the Fermi energy E_F. Since the metallicity parameter barely crosses the MIR limit, only electrons in a small range around E_F are mobile. In contrast, electrons at lower energies of the conduction band are located in the mobility gap and therefore become localized at low temperatures. The carrier localization is supported by the comparison between the Fermi surface size and the Hall density. The carrier density filling the Fermi sphere can be estimated as $n_{FS} = \frac{k_F^x \cdot k_F^y \cdot k_F^z}{3\pi^2} = 3.8 \times 10^{18}$ cm^{-3}, almost three orders of magnitude larger than the Hall density at 2.5 K (4.8×10^{15} cm^{-3}). Note that here n_{FS} only represents the volume of Fermi sphere rather than the number of mobile electrons participating in SdH oscillations. The dramatic discrepancy between n_H and n_{FS} suggests that the majority of electrons in the Fermi sphere are not counted in the Hall effect, as shown in Fig. 5b, which accounts for the deviation from the Drude model of CaAs$_3$ in Fig. 4. Only electrons beyond the mobility edge (orange region in Fig. 5b) contribute to n_H while the rest of them (blue region) are localized at 2.5 K. It could also fit with the absence of quantum oscillation in torque magnetometry. In contrast to electric transport, which directly probes the mobile electrons, the magnetization measurement contains an incoherent contribution from localized electrons, which overwhelms the dHvA oscillations (refer to Supplementary Note S6 for further discussion and simulation). Meanwhile, Landau quantization in magneto-infrared spectroscopy appears at a much larger energy scale, hence not affected by the mobility edge. The carrier localization may be responsible for the activation regime characterized by Δ_2, which corresponds to the thermal excitation of electrons from the localized state below the mobility edge to the extended state above the mobility edge [58].

Due to the opposite dispersion along Y–Γ and Y–X [20], CaAs$_3$ presents a van Hove singularity at the saddle point Y. Similar to its counterpart in 2D systems, the van Hove singularity in 3D leads to a local maximum in the DOS but with a finite value
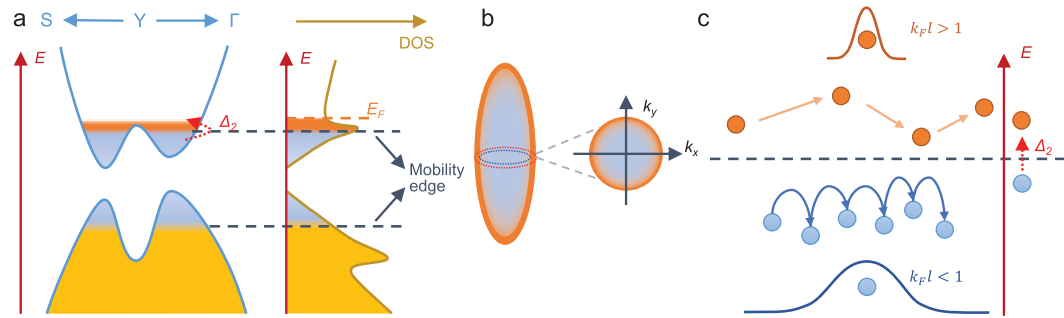
Figure 5. Schematic plots of the electronic structure and carrier transport dynamics of $CaAs_3$. (a) Sketch of the band dispersion (left) and DOS (right) in $CaAs_3$. The yellow and light blue regions separated by the mobility edge represent the extended and localized states, respectively, and the orange region corresponds to conducting carriers of the extended states near the Fermi energy E_F. (b) Sketch of the Fermi sphere. (c) The transport dynamics of the extended ($k_F l > 1$) and localized ($k_F l < 1$) states, respectively. The dashed line corresponds to the mobility edge. The red dashed arrows in (a) and (c) represent the excitation from the localized state to the extended state characterized by Δ_2.

rather than a logarithmically diverging one, as in 2D [59]. For a narrow energy window above the saddle point, the DOS decreases with the increase in energy. We verify the DOS peak near the Lifshitz transition at the saddle point in $CaAs_3$ by the DFT calculation (refer to Methods and Fig. S8). As illustrated in Fig. 5a, the Fermi level of $CaAs_3$ lies slightly above the DOS peak as well as the mobility edge. Due to the low Fermi energy, a small amount of disorder can introduce the mobility edge and lead to a metal-to-insulator transition [58]. Since the Fermi surface electrons are located in a region where the DOS decreases with E, the carriers show hole-like transport in thermoelectric measurement, resulting in the positive Seebeck coefficient at low temperatures [60]. As T increases, E_F may go beyond this narrow energy window due to the thermally excited electrons from the valence band, and the Seebeck coefficient switches back to negative. Similarly, the sign of the Hall effect is determined by the sign of Fermi velocity [60], which typically changes sign together with the slope of local DOS at the saddle point [61,62], as has been recently observed in various moiré superlattices [63,64]. However, due to the momentum and energy resolution, we do not directly resolve the Lifshitz transition by ARPES in our experiment. Other approaches such as scanning tunneling microscopy and laser-based ARPES may be utilized to study the energy dependence of the Fermi contour in this system.

Figure 5c depicts the transport dynamics of the extended ($k_F l > 1$) and localized ($k_F l < 1$) states, respectively. In the extended states, electrons move freely in the lattice with a mean free path larger than their de Broglie wavelength. This enables a quantum mechanical treatment of the electron wave function during the transport process, giving rise to vari-

ous electron-coherence phenomena such as Landau quantization and the Aharonov-Bohm effect. Electrons in the localized states are spatially confined due to the small mean free path. At low temperatures, they do not contribute to transport properties such as resistivity, Hall effect, Seebeck effect and SdH oscillations. Upon thermal activation, these localized electrons may become mobile by hopping among different sites. Unlike band transport, hopping transport does not show characteristics of the Fermi surface. In Fig. S11, we show that neither the Mott nor Efros-Shklovskii version of the variable range hopping formula can fully describe the resistivity in the low-T region. The mobility edge picture also explains the large variation of resistivity among different samples despite similar Fermi surface size (refer to Fig. S10), since the resistivity is now mainly determined by the number of mobile carriers in the extended states (orange region in Fig. 5). Despite the absence of metallicity in the temperature dependence of resistivity down to our lowest experimental temperature of 50 mK (Fig. S1b), well-defined quantum oscillations are observed in almost every $CaAs_3$ sample we measured with similar frequencies. As a direct consequence of Landau quantization, the presence of quantum oscillations is the hallmark of mobile electrons from the Fermi surface. These intrinsic mobile electrons at ground states then lead to the saturation of resistivity towards zero temperature in Fig. S11.

Perhaps the most striking finding in our study is the highly coherent electrons, which are robust enough to form cyclotron orbits, residing in the vicinity of the MIR limit. We note that other materials with small metallicity parameters such as CdTe and HgTe shown in Fig. 4 are mainly narrow-gap semiconductors with low Fermi energy and a

small k_F value. The resultant small Fermi pocket size reduces the requirement of phase-coherence length to complete the cyclotron orbit. However, distinct from these materials, $CaAs_3$ strongly deviates from the red dashed line in Fig. 4 given by the Drude model with resistivity being nearly two orders of magnitude larger. It means that the Fermi energy may lie close to the mobility gap, leaving the mobile electrons forming coherent cyclotron orbits just above the edge of Anderson localization. This peculiar behavior is reminiscent of Landau levels at finite temperatures in quantum Hall physics. Landau levels of quantum Hall systems are non-dispersive flat bands so that quantum coherence forms close to the delocalization transition. Therefore, we anticipate that the flat band around the saddle point contributes to the observed electron coherence near the mobility edge in $CaAs_3$. Although possible deviation of LK formula may occur near the quantum limit [65,66], the thermal damping factor we used to extract effective mass is less influenced by the oscillation of Fermi energy. We note that such systematic mass enhancement has not been observed in other systems such as Bi, $ZrTe_5$ and Cd_3As_2, when approaching low Landau levels [67–70]. The quasiparticle mass enhancement observed in Fig. 2 may result from the strongly suppressed mobility in magnetic fields, which further shifts the system towards the insulating side of the MIR limit.

While not excluding other possibilities, we find that the phenomenological model proposed here could account for three unconventional observations in $CaAs_3$ mentioned earlier. Further tuning of the Fermi energy may be carried out to verify the connection between the carrier sign anomaly and the van Hove singularity. It is worth noting that the proposed scenario of exotic metallic states near the mobility edge is not limited to $CaAs_3$ and is expected to appear in other low-carrier-density systems with the van Hove singularity and mobility edge near the Fermi energy as well.

CONCLUSION

To conclude, we performed a systematic quantum transport and magneto-infrared spectroscopy study of $CaAs_3$ bulk crystals. $CaAs_3$ exhibits an insulator-like temperature dependence of resistivity with a metallicity parameter close to the MIR limit. The saddle point in the band structure results in a sign reversal of Hall and Seebeck coefficients. Robust 3D SdH oscillations are observed in magnetic fields accompanied by quasiparticle mass enhancement, suggesting highly coherent band transport near the MIR limit. Distinct from the widely studied temperature dependence of resistivity, mobile electrons near the

MIR limit observed here manifest the metallic characteristic from the aspect of quasiparticle coherence. These unconventional transport properties go beyond the traditional picture of hopping conduction in the critical regime and call for further study on the electron correlation effect of the van Hove singularity at the diffusive bound.

METHODS

Crystal growth and characterization

Similar to the growth method of $SrAs_3$ in the previous study [52], $CaAs_3$ single crystals were grown by melting a stoichiometric mixture of Ca and As at 850°C. The melt was held at 850°C for 10 hours before cooling to 700°C at a rate of 2°C per hour. $CaAs_3$ bulk crystals with the *a-c* plane as the cleavage plane were then obtained after naturally cooling to room temperature. The composition and crystal structure of the as-grown crystals were checked by energy-dispersive X-ray spectroscopy and X-ray diffraction (XRD), respectively. ARPES experiments were carried out at Beamline 4.0.3 in Advanced Light Source with an energy resolution better than 15 meV. $CaAs_3$ crystals were cleaved *in situ* with a base pressure better than 1×10^{-10} Torr at 10 K.

Transport measurement

The magneto-transport measurements were performed in commercial variable temperature inserts with superconducting magnets for the low field range (0–9 T) and in resistive magnets in the Chinese High Magnetic Field Laboratory (CHMFL, China) and the National High Magnetic Field Laboratory (NHMFL, USA). The temperature dependence of the resistivity down to 50 mK was measured using a dilution refrigerator. Contact between the $CaAs_3$ crystals and the chip carrier was created using silver paints and gold wires. The typical channel size of the measured devices in transport experiments is 1.5 (length) × 1.5 (width) × 0.3 (thickness) mm^3 (Sample C1). The resistivity was measured using either the *ac* lock-in technique or the *dc* method with a current in the range of 1–100 nA applied to the sample while monitoring the voltage in the four-terminal configuration.

The thermoelectric coefficient was measured by a physical property measurement system (Quantum Design) with a home-built device. Contact between the $CaAs_3$ crystals and the chip carrier was created using silver paints and gold wires. A type-E thermocouple (Omega) was used to measure the temperature gradient and Nanovoltmeter 2182A (Keithley) was used to measure the thermoelectricity voltage.

Magnetic torque measurement

The magnetic torque was measured by capacitive cantilever in resistive magnets in CHMFL. In order to deduct the background signal from the cable and the cantilever, an empty cantilever was calibrated on the same experimental condition. Note, 0° (or 90°) in Fig. 2e is not high-symmetry crystalline axes of triclinic $CaAs_3$.

Magneto-infrared measurement

The magneto-infrared spectrum was measured in the mid-infrared range in the Faraday geometry. The spectra up to 17.5 T were measured with a super-conducting magnet at NHMFL. The spectra up to 30 T were measured with a resistive magnet at Laboratoire National des Champs Magnétiques Intenses (LNCMI), Grenoble. The infrared beam from the Fourier-transform infrared spectrometer propagates in a vacuum and is shed on the sample at a near-incident angle. The reflected beam was detected by a 4.2 K composite silicon bolometer.

Density functional theory calculations

DFT calculations were performed using the Quantum Espresso package [71]. The Perdew-Burke-Ernzerhof form of the exchange-correlation functional was used [72] and spin-orbit coupling was included. An experimentally reported structure for $CaAs_3$ was used. The Brillouin zone was sampled using an $8 \times 8 \times 8$ Monkhorst-Pack k-point grid [73]. A plane wave cut-off of 40 Ry was employed. A dense grid of $16 \times 16 \times 16$ k-points was chosen for DOS computations.

SUPPLEMENTARY DATA

Supplementary data are available at *NSR* online.

AUTHOR CONTRIBUTIONS

C.Z. and F.X. conceived the ideas and supervised the overall research. S.L. and J.W. synthetized $CaAs_3$ crystals. C.Z., Y.W., J.Z., M.Z., Y.M., Y.Z., Y.Y., P.L., Y.Z. and X.K. carried out the electric transport measurements. L.X. and Z.Z. performed the thermo-electric transport measurement. W.W. and X.Y. carried out the magneto-infrared experiments. J.Z., A.S., M.O., J.W., M.O. and L.P. helped with the transport, torque and infrared experiments at high magnetic fields. W.J., F.Z. and D.Q. conducted the photoemission experiment. C.Z. and Y.W. analyzed the data. N.B.J., Y.Z. and A.N. provided theoretical support. C.Z., Y.W., X.Y. and F.X. wrote the paper with help from all other co-authors.

Conflict of interest statement. None declared.

REFERENCES

1. Hussey NE, Takenaka K, Takagi H. Universality of the Mott–Ioffe–Regel limit in metals. *Phys Rev B* 2004; **84**: 5188–92.
2. Gunnarsson O, Calandra M, Han JE. Colloquium: saturation of electrical resistivity. *Rev Mod Phys* 2003; **75**: 1085–99.
3. Mott NF. Metal-insulator transition. *Rev Mod Phys* 1968; **40**: 677–83.
4. Anderson PW. Absence of diffusion in certain random lattices. *Phys Rev* 1958; **109**: 1492–505.
5. Greene RL, Mandal PR, Poniatowski NR *et al.* The strange metal state of the electron-doped cuprates. *Annu Rev Condens Matter Phys* 2020; **11**: 213–29.
6. Varma CM. Colloquium: Linear in temperature resistivity and associated mysteries including high temperature superconductivity. *Rev Mod Phys* 2020; **92**: 031001.
7. Phillips PW, Hussey NE, Abbamonte P. Stranger than metals. *Science* 2022; **377**: eabh4273.
8. Hayes IM, McDonald RD, Breznay NP *et al.* Scaling between magnetic field and temperature in the high-temperature superconductor $BaFe_2(As_{1-x}P_x)_2$. *Nat Phys* 2016; **12**: 916–9.

9. Yang C, Liu H, Liu Y *et al.* Signatures of a strange metal in a bosonic system. *Nature* 2022; **601**: 205–10.

10. Shen B, Zhang Y, Komijani Y *et al.* Strange-metal behaviour in a pure ferromagnetic Kondo lattice. *Nature* 2020; **579**: 51–5.

11. Bruin JAN, Sakai H, Perry RS *et al.* Similarity of scattering rates in metals showing T-linear resistivity. *Science* 2013; **339**: 804–7.

12. Grissonnanche G, Fang Y, Legros A *et al.* Linear-in temperature resistivity from an isotropic Planckian scattering rate. *Nature* 2021; **595**: 667–72.

13. Singleton J, Goddard PA, Ardavan A *et al.* Test for interlayer coherence in a quasi-two-dimensional superconductor. *Phys Rev Lett* 2002; **88**: 037001.

14. Shoenberg D. *Magnetic Oscillations in Metals.* Cambridge: Cambridge University Press, 1984.

15. Klitzing K, Dorda G, Pepper M. New method for high-accuracy determination of the fine-structure constant based on quantized Hall resistance. *Phys Rev Lett* 1980; **45**: 494–7.

16. Qu DX, Hor YS, Xiong J *et al.* Quantum oscillations and hall anomaly of surface states in the topological insulator Bi_2Te_3. *Science* 2010; **329**: 821–4.

17. Analytis JG, McDonald RD, Riggs SC *et al.* Two-dimensional surface state in the quantum limit of a topological insulator. *Nat Phys* 2010; **6**: 960–4.

18. Hartnoll SA. Theory of universal incoherent metallic transport. *Nat Phys* 2015; **11**: 54–61.

19. Xu Q, Yu R, Fang Z *et al.* Topological nodal line semimetals in the CaP_3 family of materials. *Phys Rev B* 2017; **95**: 045136.

20. Quan Y, Yin ZP, Pickett WE. Single nodal loop of accidental degeneracies in minimal symmetry: triclinic $CaAs_3$. *Phys Rev Lett* 2017; **118**: 176402.

21. Hosen MM, Dhakal G, Wang B *et al.* Experimental observation of drumhead surface states in $SrAs_3$. *Sci Rep* 2020; **10**: 2776.

22. Hrostowski HJ, Morin FJ, Geballe TH *et al.* Hall effect and conductivity of InSb. *Phys Rev* 1955; **100**: 1672–6.

23. Scott W. Electron mobility in $Hg_{1-x}Cd_xTe$. *J Appl Phys* 1972; **43**: 1055–62.

24. Xiang Z, Chen K-W, Chen L *et al.* Hall anomaly, quantum oscillations and possible Lifshitz transitions in Kondo insulator YbB12: evidence for unconventional charge transport. *Phys Rev X* 2022; **12**: 021050.

25. Pezzini S, van Delft MR, Schoop LM *et al.* Unconventional mass enhancement around the Dirac nodal loop in ZrSiS. *Nat Phys* 2018; **14**: 178–83.

26. Ramshaw BJ, Sebastian SE, McDonald RD *et al.* Quasiparticle mass enhancement approaching optimal doping in a high-*T*c superconductor. *Science* 2015; **348**: 317–20.

27. Walmsley P, Putzke C, Malone L *et al.* Quasiparticle mass enhancement close to the quantum critical point in $BaFe_2(As_{1-x}P_x)_2$. *Phys Rev Lett* 2013; **110**: 257002.

28. Chen Z-G, Chen RY, Zhong RD *et al.* Spectroscopic evidence for bulk-band inversion and three-dimensional massive Dirac fermions in $ZrTe_5$. *Proc Natl Acad Sci USA* 2017; **114**: 816–21.

29. Jiang Y, Lu Z, Gigliotti J *et al.* Valley and Zeeman splittings in multilayer epitaxial graphene revealed by circular polarization resolved magneto-infrared spectroscopy. *Nano Lett* 2019; **19**: 7043–9.

30. Akrap A, Hakl M, Tchoumakov S *et al.* Magneto-optical signature of massless Kane electrons in Cd_3As_2. *Phys Rev Lett* 2016; **117**: 136401.

31. Shao Y, Rudenko AN, Hu J *et al.* Electronic correlations in nodal-line semimetals. *Nat Phys* 2020; **16**: 636–41.

32. Russell BJ, Zhou B, Taniguchi T *et al.* Many-particle effects in the cyclotron resonance of encapsulated monolayer graphene. *Phys Rev Lett* 2018; **120**: 047401.

33. Chen Z-G, Shi Z, Yang W *et al.* Observation of an intrinsic bandgap and Landau level renormalization in graphene/boron-nitride heterostructures. *Nat Commun* 2014; **5**: 4461.

34. Laiho R, Lashkul AV, Lisunov KG *et al.* Shubnikov–de Haas effect in n-CdSb:in under pressure. *Semicond Sci Technol* 2009; **24**: 095023.

35. Obata Y, Matsuishi S, Hosono H. Flux growth and magneto-transport properties of cubic antiperovskite Ca_3PbO single crystals. *Mater Res Bull* 2018; **106**: 1–6.

36. Scholl S, Waag A, Hommel D *et al.* First evidence of Shubnikov-De Haas oscillations in CdTe. *Phys B Condens Matter* 1993; **184**: 226–8.

37. Joseph AS, Thorsen AC, Gertner E *et al.* Low-field de Haas-van Alphen effect in copper. *Phys Rev* 1966; **148**: 569–75.

38. Maruhashi K, Takahashi KS, Bahramy MS *et al.* Anisotropic quantum transport through a single spin channel in the magnetic semiconductor $EuTiO_3$. *Adv Mater* 2020; **32**: 1908315.

39. Zhang J, Chen J, Li P *et al.* Topological electronic state and anisotropic Fermi surface in half-Heusler GdPtBi. *J Phys Condens Matter* 2020; **32**: 355707.

40. Justice RJ, Seiler DG, Zawadzki W *et al.* Characterization of molecular-beam epitaxially grown HgTe films by Shubnikov–de Haas measurements. *J Vac Sci Technol A* 1988; **6**: 2779–84.

41. Xiong J, Kushwaha S, Krizan J *et al.* Anomalous conductivity tensor in the Dirac semimetal Na_3Bi. *Europhys Lett* 2016; **114**: 27002.

42. Stephens AE, Miller RE, Sybert JR *et al.* Shubnikov-de Haas effect in n-InAs and n-GaSb. *Phys Rev B* 1978; **18**: 4394–401.

43. Luo Y, Ghimire NJ, Wartenbe M *et al.* Electron-hole compensation effect between topologically trivial electrons and nontrivial holes in NbAs. *Phys Rev B* 2015; **92**: 205134.

44. Stephens AE, Seiler DG, Sybert JR *et al.* Determination of the g factor from unsplit Shubnikov-de Haas oscillations in n-InSb. *Phys Rev B* 1975; **11**: 4999–5001.

45. Beckman O and Shapira Y. Quantum oscillations in the ultrasonic absorption in p-type PbSe. *Phys Lett* 1966; **21**: 282–3.

46. Kawakatsu S, Nakaima K, Kakihana M *et al.* De Haas–van Alphen oscillations for small electron pocket Fermi surfaces and huge H-linear magnetoresistances in degenerate semiconductors PbTe and PbS. *J Phys Soc Jpn* 2019; **88**: 013704.

47. Lin X, Bridoux G, Gourgout A *et al.* Critical doping for the onset of a two-band superconducting ground state in $SrTiO_{3-\delta}$. *Phys Rev Lett* 2014; **112**: 207002.

48. Wang W, Du Y, Xu G *et al.* Large linear magnetoresistance and Shubnikov-de Hass oscillations in single crystals of YPdBi Heusler topological insulators. *Sci Rep* 2013; **3**: 1–7.

49. Butch NP, Syers P, Kirshenbaum K *et al.* Superconductivity in the topological semimetal YPtBi. *Phys Rev B* 2011; **84**: 220504.

50. Liang T, Gibson Q, Ali MN *et al.* Ultrahigh mobility and giant magnetoresistance in the Dirac semimetal Cd_3As_2. *Nat Mater* 2015; **14**: 280–4.

51. Zhang C-L, Yuan Z, Jiang Q-D *et al.* Electron scattering in tantalum monoarsenide. *Phys Rev B* 2017; **95**: 085202.

52. Li S, Guo Z, Fu D *et al.* Evidence for a Dirac nodal-line semimetal in $SrAs_3$. *Sci Bull* 2018; **63**: 535–41.

53. Mackenzie AP, Julian SR, Sinclair DC *et al.* Normal-state magnetotransport in superconducting $Ti_2Ba_2CuO_{6+\delta}$ to millikelvin temperatures. *Phys Rev B* 1996; **53**: 5848–55.

54. Vignolle B, Carrington A, Cooper RA *et al.* Quantum oscillations in an overdoped high-Tc superconductor. *Nature* 2008; **455**: 952–5.

55. Kushwaha P, Sunko V, Moll Philip JW *et al.* Nearly free electrons in a 5d delafossite oxide metal. *Sci Adv* 2015; **1**: e1500692.

56. Tan BS, Hsu Y-T, Zeng B *et al.* Unconventional Fermi surface in an insulating state. *Science* 2015; **349**: 287–90.

57. Xiang Z, Kasahara Y, Asaba T *et al.* Quantum oscillations of electrical resistivity in an insulator. *Science* 2018; **362**: 65–9.

58. Mott N. Conductivity, localization, and the mobility edge. In: Joannopoulos JD and Lucovsky G (eds). *The Physics of Hydrogenated Amorphous Silicon II* Vol **56**. Berlin, Heidelberg: Springer Berlin Heidelberg, 1984, 169–93.

59. Xu S-Y, Liu C, Belopolski I *et al.* Lifshitz transition and Van Hove singularity in a three-dimensional topological Dirac semimetal. *Phys Rev B* 2015; **92**: 075115.

60. Datta S. *Lessons from Nanoelectronics.* Singapore: World Scientific, 2011.

61. Maharaj AV, Esterlis I, Zhang Y *et al.* Hall number across a van Hove singularity. *Phys Rev B* 2017; **96**: 045132.

62. Herman F, Buhmann J, Fischer MH *et al.* Deviation from Fermi-liquid transport behavior in the vicinity of a Van Hove singularity. *Phys Rev B* 2019; **99**: 184107.

63. Park JM, Cao Y, Watanabe K *et al.* Tunable strongly coupled superconductivity in magic-angle twisted trilayer graphene. *Nature* 2021; **590**: 249–55.

64. Wu S, Zhang Z, Watanabe K *et al.* Chern insulators, van Hove singularities and topological flat bands in magic-angle twisted bilayer graphene. *Nat Mater* 2021; **20**: 488–94.

65. Küppersbusch C and Fritz L. Modifications of the Lifshitz-Kosevich formula in two-dimensional Dirac systems. *Phys Rev B* 2017; **96**: 205410.

66. Guo C, Alexandradinata A, Putzke C *et al.* Temperature dependence of quantum oscillations from non-parabolic dispersions. *Nat Commun* 2021; **12**: 6213.

67. Édel'man VS. Electrons in bismuth. *Adv Phys* 1976; **25**: 555–613.

68. Krasovitsky V. Quantum oscillations of Bi and alloy BiSb magnetoresistance in magnetic fields up to 33 T. *Phys B Condens Matter* 2003; **329–33**: 1099–100.

69. Liu Y, Yuan X, Zhang C *et al.* Zeeman splitting and dynamical mass generation in Dirac semimetal $ZrTe_5$. *Nat Commun* 2016; **7**: 12516.

70. Zhao Y, Liu H, Zhang C *et al.* Anisotropic Fermi surface and quantum limit transport in high mobility three-dimensional dirac semimetal Cd_3As_2. *Phys Rev X* 2015; **5**: 031037.

71. Giannozzi P, Baroni S, Bonini N *et al.* QUANTUM ESPRESSO: a modular and open-source software project for quantum simulations of materials. *J Phys Condens Matter* 2009; **21**: 395502.

72. Perdew JP, Burke K, Ernzerhof M. Generalized gradient approximation made simple. *Phys Rev Lett* 1996; **77**: 3865–8.

73. Monkhorst HJ and Pack JD. Special points for Brillouin-zone integrations. *Phys Rev B* 1976; **13**: 5188–92.